Avalanche effects near nanojunctions

Vishal V. R. Nandigana and N. R. Aluru[*]

Department of Mechanical Science and Engineering, Beckman Institute for Advanced Science and Technology,
University of Illinois at Urbana-Champaign, Urbana, Illinois 61801, USA

In this article, we perform a computational investigation of a nanopore connected to external fluidic reservoirs of asymmetric geometries. The asymmetry between the reservoirs is achieved by changing the cross-sectional areas, and the reservoirs are designated as the micropore reservoir and macropore reservoir. When an electric field is applied, which is directed from the macropore towards the micropore reservoir, we observe local nonequilibrium chaotic current oscillations. The current oscillations originate at the micropore-nanopore interface owing to the local cascade of ions; we refer to this phenomenon as the "avalanche effects." We mathematically quantify chaos in terms of the maximum Lyapunov exponent. The maximum Lyapunov exponent exhibits a monotonic increase with the applied voltage and the macropore reservoir diameter. The temporal power spectra maps of the chaotic currents depict a low-frequency "$1/f$"-type dynamics for the voltage chaos and "$1/f^2$"-type dynamics for the macropore reservoir chaos. The results presented here offer avenues to manipulate ionic diodes and fluidic pumps.

I. INTRODUCTION

Nanofluidic devices have witnessed a tremendous surge in recent years [1,2], with applications ranging from single molecule sensing [3,4], to DNA sequencing [5–8], to water desalination [9]. However, fabricating a single nanopore with finite precision is often a challenging task. Oftentimes hundreds of thousands to millions of nanometer-sized pores [see Fig. 1(a)] are exposed to a microfluidic reservoir filled with saline solution [10–13]. To a large extent, the physics of these systems can be understood by considering a single nanopore connected to microfluidic reservoirs. Under the application of an electric field, the ionic solution is driven through the nanopore, and ionic current measurements are recorded as an output. Recent experiments by Miller *et al.* [10] and Wang *et al.* [11] revealed that ionic current can be rectified when a polycarbonate track etched nanoporous membrane is integrated with an asymmetric microfluidic reservoir geometry. These membranes were suggested as potential ionic diodes. The asymmetry between the reservoirs was achieved by changing their cross-sectional areas. The reservoir asymmetry along with the polarity-dependent propagation of the enriched and depleted concentration polarization zones were identified as the fundamental mechanisms for current rectification. The primary advantage of these diodes over other ionic diodes [14,15] is to avoid manipulating the geometry of the nanopore or the surface chemistry of the nanopore to rectify the current.

The experimental work of Wang *et al.* [11] also observed oscillations in the output current upon systematic increase in the degree of asymmetry between the fluidic reservoirs and at larger bias voltages. The chaotic current oscillations were predominantly observed when the applied electric field is directed from the macropore towards the micropore reservoir (ON state). The exact physical mechanism behind the current oscillations in their experiments is still unclear. However, several mechanisms are postulated for the nonequilibrium current fluctuations and oscillations in nanoporous membranes. Powell *et al.* [16] attributed the current fluctuations to the

dynamical changes in the ionic diffusivity and the corresponding ionic mobility. Other mechanisms include nanopore wall surface charge fluctuations [17], conformational changes of the pore structural constituents [18], nanobubble formation inside the nanopore [19], and water splitting [20]. Furthermore, strong concentration polarization effects resulting in depletion of ions near the interfaces of micropore-nanopore integrated systems have resulted in instability of ionic charges and correspondingly in electro-osmotic flow near these interfaces. These instabilities were also argued to be the source of chaotic current oscillations [21–26].

In this article, we perform numerical simulations of a single nanoporous membrane connected to asymmetric reservoirs of a few hundreds of nanometers to examine the experimental findings of Wang *et al.* [11]. The two asymmetric reservoirs are denoted as the micropore and macropore reservoirs. When an electric field is applied from the macropore to the micropore reservoir (ON state), we observe chaotic current oscillations. We show that the current oscillations are due to the coupling between the electric field and the enriched concentration zone observed at the entrance of the micropore-nanopore junction. The dynamical cascading or clustering of ions, referred to as "avalanche effects," near the enriched micropore-nanopore junction leads to temporal changes in the electric potential, which in turn results in unstable or chaotic currents. We demonstrate that the strong clustering of ions is due to the introduction of an asymmetry in the fluidic reservoirs. Our observations are analogous to the financial price dynamics [27] and escape panic dynamics [28]. The price and traffic cascadement is due to the memory effects in the system owing to a random memory force. However, in this article, the dynamic cascadement of ions presumes a deterministic long-range electrostatic force near the external microporous environment in conjunction with a nanoporous membrane. We mathematically quantify chaos in terms of the maximum Lyapunov exponent. We observe a positive Lyapunov exponent augmenting instability or chaos. Furthermore, we demonstrate the temporal power spectra map of the numerical chaos and draw conclusions on the dominant source of chaos from our power spectral density analysis.

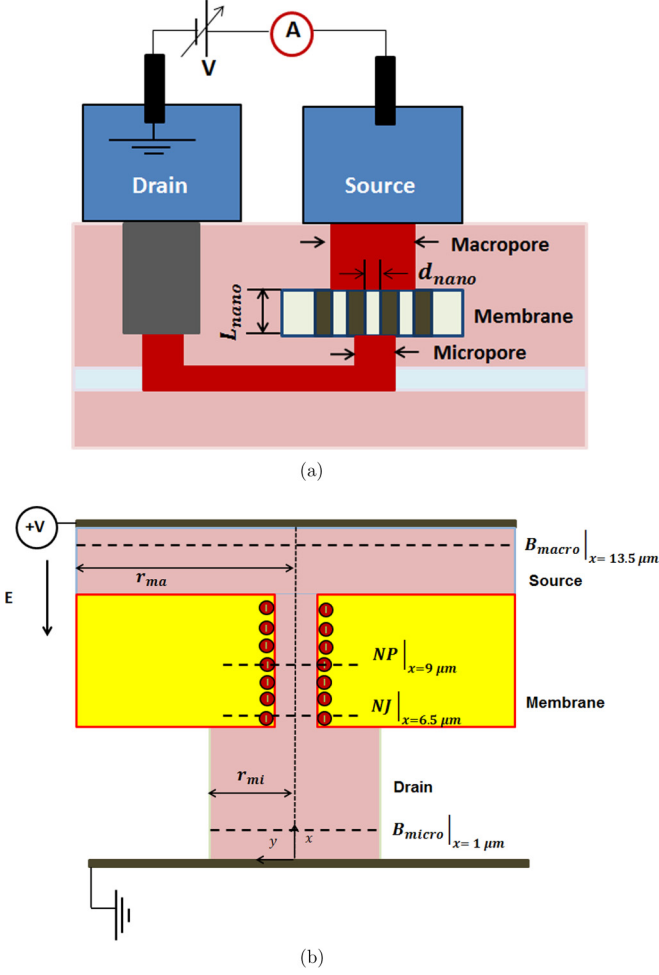[*]aluru@illinois.edu; http://www.illinois.edu/~aluru

FIG. 1. (a) Schematic illustration of multiple nanopores interacting with asymmetric fluidic reservoirs (b) Simulation setup of a single micro-nano-macropore system. The electric field is applied from macropore to micropore reservoir. Ionic current is calculated at four different regions: at bulk micropore reservoir (B_{micro}, $x = 1\,\mu\text{m}$ from the origin), nanopore junction (NJ) at a distance of $0.5\,\mu\text{m}$ from the micropore-nanopore entrance, center of the nanopore (NP, $x = 9\,\mu\text{m}$ from the origin), and bulk macropore reservoir (B_{macro}, $x = 13.5\,\mu\text{m}$).

II. THEORY

To understand the ion transport dynamics in a microreservoir-nanopore-macroreservoir system (hereafter simply referred to as micro-nano-macrosystem), we compute the axial changes in the potential (ϕ) and ionic concentration (c_i) using the area-averaged multi-ion transport model (AAM). A detailed derivation of the model is discussed in our earlier work [29], and in this section we present a concise summary of the model. We consider the 2D Poisson-Nernst-Planck equations and assume ideal nonpolarizable electrodes; i.e., Faradaic reactions are neglected. The medium is assumed to be isotropic with a constant dielectric permittivity, $\epsilon = \epsilon_0 \epsilon_r$. ϵ_0 is the permittivity of free space and ϵ_r is the relative permittivity of the medium. Furthermore, assuming that ions are held rigidly in the steric layer [30], the contribution of steric current to the total current is neglected. Under these assumptions, the

mass transfer of each species in the solution is given by

$$\frac{\partial c_i}{\partial t} = -\nabla \cdot \mathbf{\Gamma}_i, \tag{1}$$

where $\mathbf{\Gamma}_i$ is the total flux of each species i in the solution,

$$\mathbf{\Gamma}_i = -D_i \nabla c_i - \Omega_i z_i F c_i \nabla \phi, \tag{2}$$

where D_i, c_i, and z_i denote the diffusion coefficient, molar concentration, and valence of each ion, respectively. Ω_i is the ionic mobility which is related to the diffusion coefficient by Einstein's relation [31], $\Omega_i = \frac{D_i}{RT}$. F, R, and T represent Faraday's constant, ideal gas constant, and absolute thermodynamic temperature, respectively. We assume c_i and ϕ to be uniform in the θ direction. Integrating Eq. (1) over the (r, θ) direction and normalizing with the cross-sectional area, $A(x)$, the transport of each ion, i, in the axial direction can be calculated as

$$\frac{1}{A(x)} \int_0^R \int_0^{2\pi} \left(\frac{\partial c_i}{\partial t} \right) r \, dr \, d\theta$$
$$= \int_0^R \int_0^{2\pi} \left\{ \frac{\partial}{\partial x} \left[\frac{1}{A(x)} D_i \frac{\partial c_i}{\partial x} + \frac{z_i D_i F}{RT} \frac{1}{A(x)} c_i \frac{\partial \phi}{\partial x} \right] \right\} r \, dr \, d\theta$$
$$+ \frac{1}{A(x)} \int_0^R \int_0^{2\pi} \left[\frac{1}{r} \frac{\partial}{\partial r} \left(D_i r \frac{\partial c_i}{\partial r} + \frac{D_i z_i F}{RT} r c_i \frac{\partial \phi}{\partial r} \right) \right] r \, dr \, d\theta, \tag{3}$$

R is the radius of the pore, varying along the axial direction, representing the micropore, nanopore, and macropore radius along the axial direction. The cross-sectional area of each pore (micro-, nano-, and macro-), $A(x)$, varies along the axial flow direction. Since there is no leakage of ionic current at the pore walls, the normal flux of each ion on the pore walls is assumed to be zero,

$$\mathbf{n}_w \cdot \mathbf{\Gamma}_i|_{r=R} = -D_i \frac{\partial c_i}{\partial r}\bigg|_{r=R} - \left(\frac{z_i D_i F}{RT} c_i \frac{\partial \phi}{\partial r} \right)\bigg|_{r=R} = 0, \tag{4}$$

where $\mathbf{n}_w$ denotes the unit normal vector (pointing outwards) to the pore surface. Substituting the above condition in Eq. (3), we obtain the area-averaged transport equation for the ionic species,

$$A(x) \frac{\partial \hat{c}_i}{\partial t} = \frac{\partial}{\partial x} \left[A(x) D_i \frac{\partial \hat{c}_i}{\partial x} \right] + \frac{\partial}{\partial x} \left[\frac{z_i D_i F}{RT} A(x) \hat{c}_i \frac{\partial \hat{\phi}}{\partial x} \right]; \tag{5}$$

$\hat{f} = \frac{1}{A} \int_0^r \int_0^{2\pi} [f(r, \theta)] r \, d\theta \, dr$ denotes the area-averaged quantity. The first term on the right-hand side accounts for the ionic diffusive effects, while the second term accounts for the electromigration effects inside the system.

We now consider the 2D Poisson equation for the electric field distribution,

$$\nabla \cdot (\epsilon_r \nabla \phi) = -\frac{\rho_e}{\epsilon_0}, \tag{6}$$

where ρ_e is the net space charge density of the ions defined as $\rho_e = F(\sum_{i=1}^n z_i c_i)$, where n is the number of ionic species in the solution. Applying the charge conservation at the walls

leads to the electrostatic boundary condition

$$\mathbf{n} \cdot \nabla \phi = \frac{\sigma}{\epsilon},$$ (7)

where $\mathbf{n}$ denotes the unit normal vector (pointing outwards) to the wall surface and σ is the surface charge density of the walls. Invoking the assumption that ϕ is uniform in the θ direction and integrating Eq. (6) over the (r,θ) and substituting Eq. (7), we obtain the governing equation for the radially averaged electrostatic potential in the axial direction,

$$\frac{\partial}{\partial x}\left[A(x)\frac{\partial\hat{\phi}}{\partial x}\right] = -\frac{A(x)}{\epsilon}\left[\hat{\rho}_e + \frac{4\sigma_s(x)}{d(x)}\right],$$ (8)

where $\sigma_s(x)$ and $d(x)$ are the fixed surface charge density and the diameter of the pore. Both these quantities vary axially to incorporate the surface and geometrical properties of the micro-, nano-, and macropores. The fixed wall surface charge density distribution, $\sigma_s(x)$, is given by

$$\sigma_s(x) = \begin{cases} \sigma_{mi}, & 0 \leqslant x \leqslant L_{mi} \\ \sigma_n, & L_{mi} < x \leqslant L_{mi} + L_n \\ \sigma_{ma}, & L_{mi} + L_n < x \leqslant L_{mi} + L_n + L_{ma}, \end{cases}$$ (9)

where σ_{mi}, σ_n, and σ_{ma} denote the homogeneous charge distribution on the walls of the micro-, nano-, and macropore, respectively. L_{mi}, L_n, and L_{ma} refer to the length of the micro-, nano-, and macropore, respectively.

The total ionic current, $I(x)$, through the pore is calculated by summing the individual fluxes over the cross-sectional area,

$$I(x) = FA(x)\sum_i^n z_i\Gamma_i,$$ (10)

where $\Gamma_i = -D_i\frac{\partial\hat{c}_i}{\partial x} - \frac{z_iFD_i}{RT}\hat{c}_i\frac{\partial\hat{\phi}}{\partial x}$ is the total area-averaged flux of each ionic species, with the diffusive component (first term on the right-hand side) resulting from the concentration gradient, and the migration component (second term on the right-hand side) is due to the electric field interaction with the ionic concentration.

The closure of the problem requires boundary conditions. We consider the macropore [see Fig. 1(b)] as the source and a constant electric potential (ϕ_{DC}) is specified as the boundary condition at the end of the macropore reservoir. The micropore is considered as the drain and is grounded. The concentration of both the ions at the ends of the micro- and macropore is assumed to be equal to the bulk ionic concentration, c_0. The solvers for the AAM model are developed and implemented using the finite volume method in OpenFOAM (Open Field Operation and Manipulation) version 1.6 [32]. The electromigration terms in the AAM model are discretized using the second-order bounded NVD schemes [33] to avoid artificial oscillations and to ensure that the solution is bounded. All the Laplacian terms are discretized using the second-order central differencing scheme. Second-order implicit time differencing scheme [32] is used to discretize the variables in time. A finer mesh is introduced at the entrance and exit of the nanopore to resolve the features of the thin electrical double layer near the interfaces.

III. SIMULATION DETAILS

We consider a cylindrical nanopore of length $L_n = 6\,\mu m$ and diameter $d_n = 10\,nm$. The nanopore is connected to a micropore of length $L_{mi} = 6\,\mu m$ and diameter $d_{mi} = 50\,nm$, and a macropore of length, $L_{ma} = 2\,\mu m$. The macropore diameter (d_{ma}) is systematically varied from 50 nm to 1 μm. For the smallest macropore diameter considered, the ratio of macropore to micropore reservoir diameter ($R = d_{ma}/d_{mi}$) is 1 (symmetric reservoirs), and for the largest macropore diameter considered, we ensure a 20-fold difference between the two reservoir diameters (asymmetric reservoirs). We would like to note that though the reservoir diameters are in the range of nanometers, we designate them as micropore and macropore to distinguish the reservoir geometry. The voltage is systematically varied from 5 to 100 V and is always directed from the macropore towards the micropore. Phosphate buffer of constant concentration (0.39 mM of NaH_2PO_4 and 0.61 mM of Na_2HPO_4) is used in all the simulations. The simulated temperature is $T = 300$ K. The diffusivities of Na^+, $H_2PO_4^-$, and HPO_4^{2-} are $1.33 \times 10^{-9}\,m^2/s$, $0.879 \times 10^{-9}\,m^2/s$, and $0.439 \times 10^{-9}\,m^2/s$, respectively. The dielectric constant of the aqueous solution is assumed to be $\epsilon_r = 80$ [34]. The nanopore is modeled with a homogeneous negative surface charge density, $\sigma_n = -3\,mC/m^2$, which is the typical surface charge density of a poly-carbonate track etched (PCTE) membrane, when an electrolyte concentration of 1 mM is used [35]. We assume that the surface charge density on the walls of the micropore and macropore reservoirs are zero ($\sigma_{mi} = \sigma_{ma} = 0$), as they are far away from the nanopore to have an influence on the ion transport.

IV. RESULTS AND DISCUSSION

A. Current-time dynamics

A schematic illustration of the micro-nano-macropore simulation setup is shown in Fig. 1(b). We calculate the conductive currents at four different locations: in the bulk micropore reservoir, B_{micro} at $x = 1\,\mu m$, at the micropore-nanopore junction, NJ, $x = 6.5\,\mu m$ (which is 0.5 μm from the entrance of the micro-nanopore), center of the nanopore, NP, $x = 9\,\mu m$, and at the bulk macropore reservoir, B_{macro}, $x = 13.5\,\mu m$ [see Fig. 1(b)]. Figure 2(a) shows that the micro-nano-macropore system exhibits a non-Ohmic current-voltage characteristic. The magnitude of the output current, $|\langle I\rangle|$ is calculated at the center of the nanopore (NP region) and is averaged over 4 ms time interval after the current reaches a steady state. For this calculation, the ratio of macropore to micropore diameter is 4. Recent experimental studies by Kim *et al.* [22] and Yossifon *et al.* [23,24] have also observed similar non-Ohmic current-voltage characteristics in a micro-nanopore integrated system. In our earlier work [29,36], we have shown that the non-Ohmic current characteristics are due to the concentration polarization effects developed near the micro-nanopore junctions. The current-voltage characteristics shown in Fig. 2(a) reveal the average transport properties of the pore. In order to understand the dynamic characteristics of the current, we analyze the current-time signals. The slowest relaxation mechanism in the system is the diffusion process, whose characteristic time is ($L_{nano}^2/2D_{ion}$), where $L_{nano} = 6\,\mu m$ is the length of the
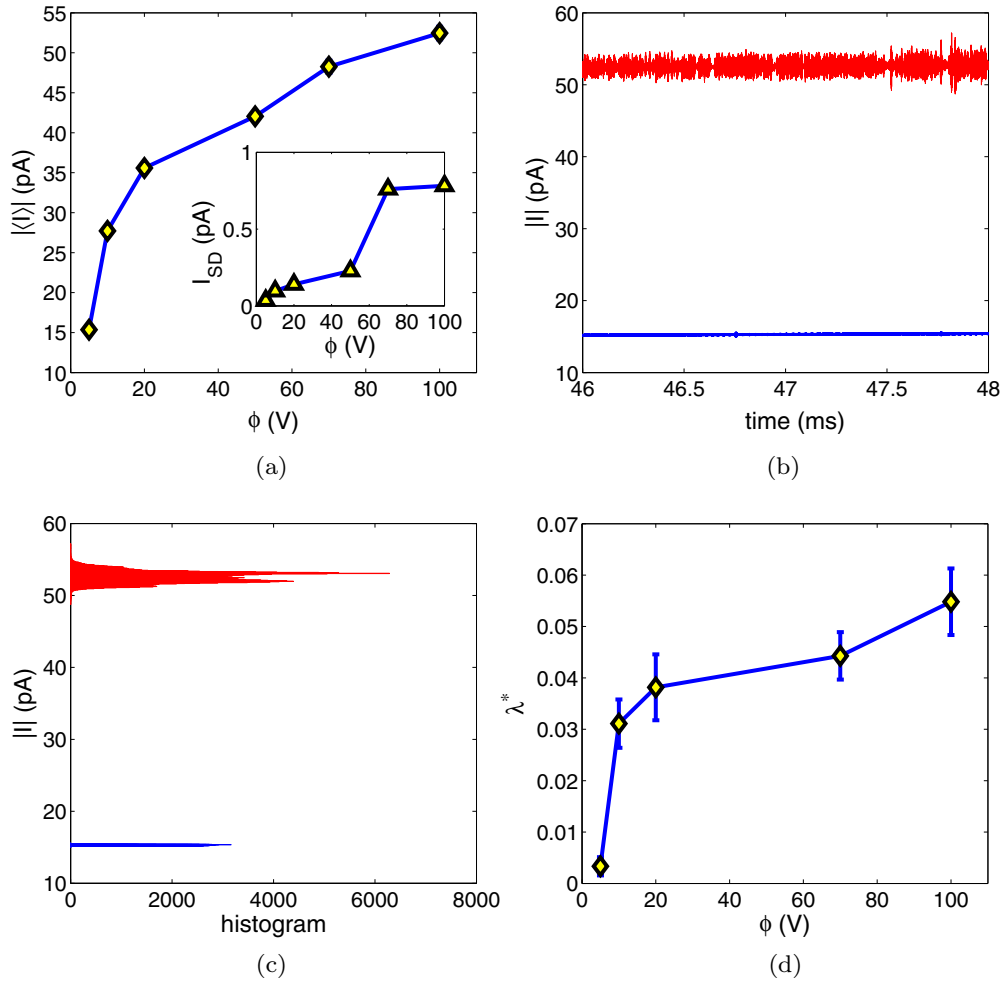
FIG. 2. Variation of the output current (in magnitude) at the center of the nanopore with (a) applied voltage (current is averaged over 4 ms time interval for each voltage); inset shows the variation of the standard deviation of the current over the time interval considered for each voltage, (b) time (data shown for the last 2 ms), and (c) its corresponding histogram for 5 V (solid blue line) and 100 V (solid red line), respectively. (d) Variation of the maximum Lyapunov exponent with applied voltage. The ratio of macropore to micropore reservoir diameter is 4 in (a) to (d).

nanopore and D_{ion} corresponds to $D_{(HPO_4^{2-})}$ as it has the smallest diffusion coefficient, $D_{(HPO_4^{2-})} = 0.439 \times 10^{-9}\,\mathrm{m}^2/\mathrm{s}$. Thus, the ions inside the nanoporous membrane require approximately 41 ms to relax and reach a steady state. To characterize the long time dynamics of the system, we run the simulations, for each voltage case, at least till 48 ms with a sampling frequency of 100 MHz to ensure that the current oscillates about a steady mean.

Figure 2(b) shows current-time dynamics from 46 ms to 48 ms for an applied voltage of 5 V, corresponding to the quasi-equilibrium regime, and for 100 V, corresponding to the highly nonequilibrium regime. The current trace was obtained at the center of the nanopore structure [shown as region NP in Fig. 1(b)]. We observe weak oscillations in the current trace for the low voltage, while there is a high degree of oscillations in the current signal for the 100 V case. To quantify the differences between the two signals, Fig. 2(c) shows the current histogram. We notice a peak in the histogram at 15.36 pA, with a spread of 0.2 pA for the quasi-equilibrium voltage of 5 V, while the 100 V case

results in a spread of 3–4 pA in the current histogram [see Fig. 2(c)]. To mathematically quantify the nonequilibrium current oscillations, we calculate the growth rate given by the maximum Lyapunov exponent (λ^*) for each voltage. The mathematical details for the implementation of λ^* are discussed in the Appendix. λ^* is normalized as we consider the time scale in the units of time index of measurements and not the real time units. We use the TISEAN software package [37] to calculate λ^*. Figure 2(d) reveals a positive Lyapunov exponent for all the voltages considered. A positive Lyapunov exponent indicates a positive growth rate indicating unstable current dynamics inside the nanopore system. λ^* is 0.003 ± 0.001 for 5 V, and it increases monotonically with voltage, reaching a value of 0.055 ± 0.006 at 100 V. We postulate the monotonic increase in λ^* to the monotonic increase in the standard deviation of the current signal (I_{SD}) with voltage [see inset of Fig. 2(a)]. The exact correlation between I_{SD} and λ^* is still unclear and is subject of subsequent study.

Next, we examined the effect of asymmetry of reservoirs, characterized by $R(= d_{ma}/d_{mi})$, on the output current for an
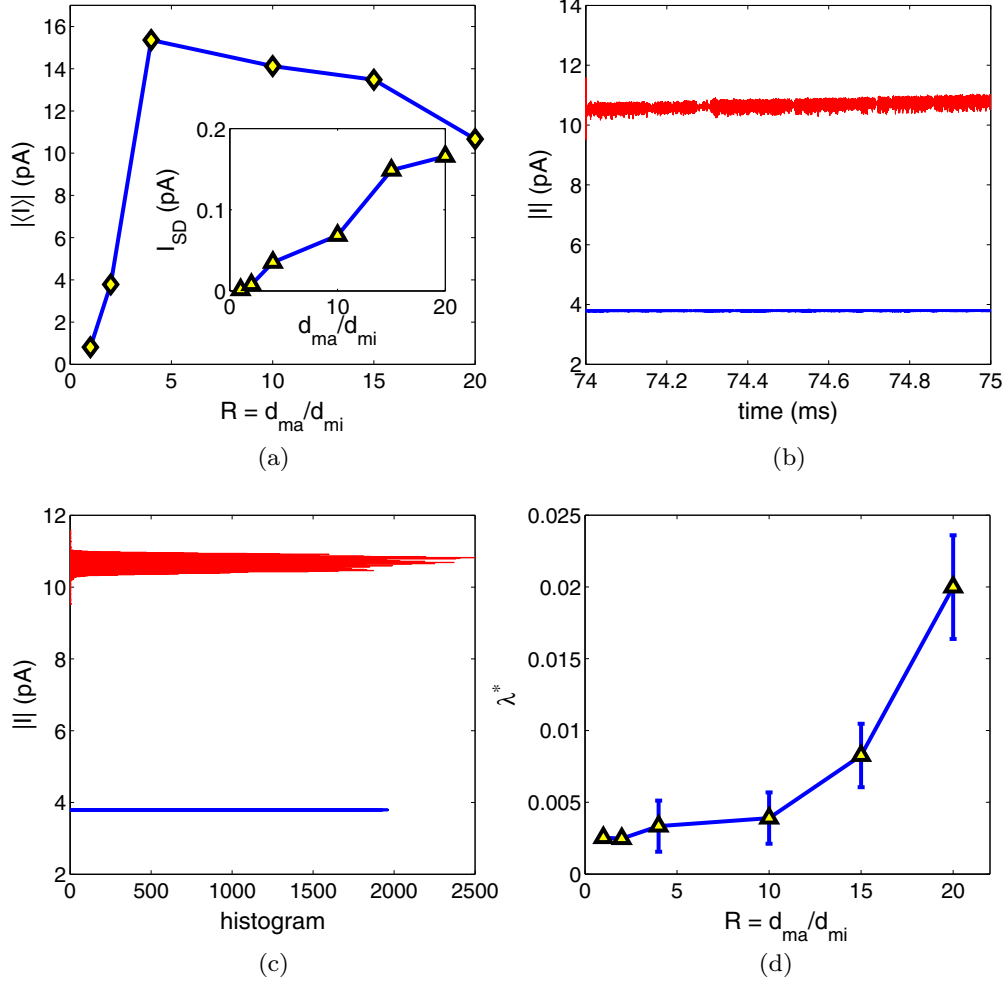
FIG. 3. Variation of the output current (in magnitude) with (a) macropore to micropore radius ($R = d_{ma}/d_{mi}$), current averaged over 4 ms time interval for each R); inset shows the variation of the standard deviation of the current, over the time interval considered for each R, (b) time (data shown for the last 1 ms), and (c) its corresponding histogram for $R = 2$ (solid blue line) and $R = 20$ (solid red line), respectively. (d) Variation of the maximum Lyapunov exponent with R. The applied voltage is 5 V, and the micropore reservoir diameter is 0.05 μm in (a) to (d).

applied bias of 5 V. To vary R, we increase the macropore reservoir diameter keeping the micropore reservoir diameter and nanopore diameter fixed. Figure 3(a) shows that the magnitude of the average output current varies nonmonotonically with R and reaches a maximum at $R = 4$. The output current, $|\langle I \rangle|$, is calculated at the center of the nanopore [NP region; see Fig. 1(b)] and is averaged over a 4 ms time interval after the current reached the steady state. This result is indeed interesting as one would expect a monotonic increase in current, I, with cross-sectional area. However, our calculations show that the concentration of ions inside the nanopore vary nonmonotonically with R affecting the current characteristics. A maximum concentration of Na$^+$ ions inside the nanopore was observed for $R = 4$ where the current was found to be maximum. Figure 3(b) shows the current-time dynamics, for $R = 2$ and 20 for an applied bias of 5 V. For $R = 20$, we observe a high degree of current oscillations of the order of 0.8 pA, while weak oscillations of the order of 0.025 pA were observed for $R = 2$ [see Fig. 3(c)]. The high degree of current oscillations for large R is quite surprising as a low

bias voltage of 5 V is applied in this case. To understand these results, we again calculated the maximum Lyapunov exponent. Figure 3(d) reveals a positive Lyapunov exponent for all R. λ^* is 0.0024 for $R = 2$ and it monotonically increases with R, reaching 0.02 ± 0.004 at $R = 20$. We again postulate the monotonic increase in the maximum Lyapunov exponent to the monotonic increase in the standard deviation of the current I_{SD} with R [see inset of Fig. 3(a)]. This analysis helps us to conclude that the asymmetric nature of the fluidic reservoirs plays a vital role compared to the applied voltage in observing large current oscillations in the nanopore systems.

Before highlighting the mechanism behind the current oscillations observed in our study, we briefly discuss different sources of current oscillations postulated in the literature. Powell *et al.* [16] correlated the dynamical changes in the ion diffusion coefficient and its corresponding ionic mobility to be the source of current oscillations. In another study, the dynamical change of the surface charge density on the pore walls due to constant protonation and deprotonation reactions [38] was suggested to be the source of current oscillations.
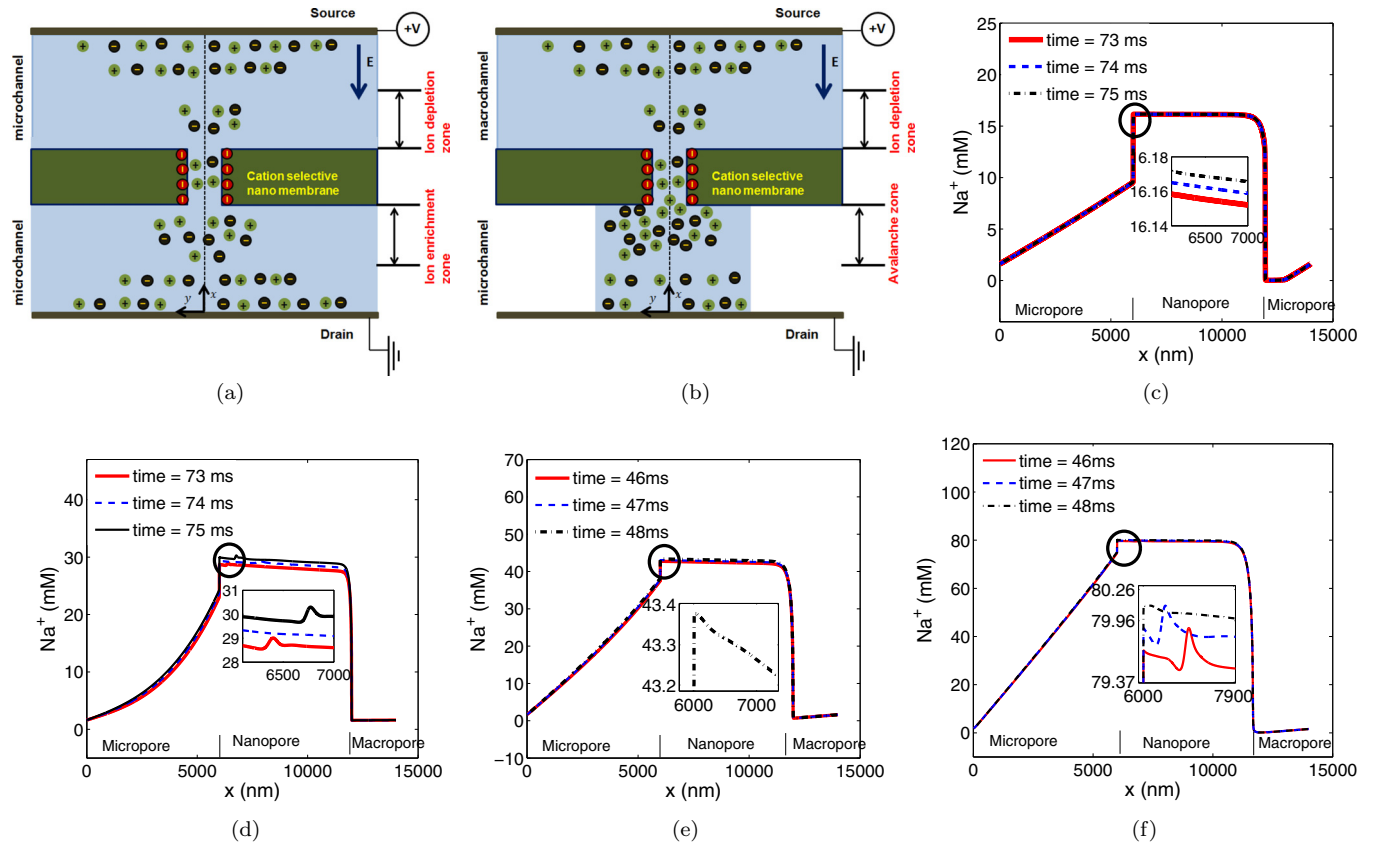
FIG. 4. Avalanche effect mechanism for (a) a symmetric reservoir ($R = 1$), ions are enriched near the drain micropore-nanopore interface and an ion depletion zone is developed near the source micropore-nanopore interface. (b) An asymmetric reservoir ($R > 1$), cluster of ions accumulate near the micropore-nanopore interface, an "avalanche zone" is created, and a relatively weak ion depletion zone is developed near the nanopore-macropore interface. Concentration distribution of sodium ions (counterions) along the micro-nano-macropore reservoir system for (c) 5 V and $R = 1$, inset reveals distribution of an ion enriched zone; (d) 5 V and $R = 20$, inset reveals dynamic clustering of ions near the micropore-nanopore interface; (e) 5 V and $R = 4$, inset reveals weak oscillation of ions near the enriched zone; and (f) 100 V and $R = 4$, inset reveals strong enrichment of ions and an inhomogeneous distribution of ions near the enriched micropore-nanopore interface.

In this study, we used a constant surface charge density and a time-independent diffusion coefficient for all the ions. Hence, we rule out these postulations for the source of current oscillations observed in our study.

B. Dynamic cascading of ions

In order to investigate the mechanism, we calculated the ionic concentration distribution along the entire micro-nano-macropore system. For a symmetric reservoir ($R = 1$), under the action of an applied voltage from the source reservoir to the drain reservoir [see Fig. 4(a)], the co-ions (anions in this case) are repelled from the source-nanopore interface and are attracted towards the anode. In order to maintain electro-neutrality, the cations are also repelled at this interface. Hence an ion depletion zone is created at the source-nanopore interface. Further, the co-ions are repelled from both the cathode and from the nanopore (as the pore is negatively charged), and they get accumulated near the drain-nanopore interface. In order to maintain electro-neutrality, the cations (counterions) also get accumulated at this interface. Thus the ions are polarized near both the interfaces. For a symmetric reservoir case, the cascading or enrichment of ions is relatively

weak. However, when the size of the reservoirs is asymmetric, we observe a high clustering of ions in the ion enrichment zone. We call this region the "avalanche zone" [see Fig. 4(b)].

Figure 4(c) shows the sodium ion concentration distribution for the symmetric reservoir system. In the case of a symmetric reservoir for 1 mM bulk concentration, applied voltage of 5 V, and for $R = 1$, we observe around 15-fold enrichment near the drain micropore-nanopore interface. Furthermore, the long time dynamics reveal weak oscillations of ionic concentration distribution under the low bias voltage, near the enriched drain micropore-nanopore interface. However, for an asymmetric reservoir, when we introduce a 20-fold difference in the reservoir diameter ($R = 20$), we observe 30 times enrichment of ionic concentration near the drain micropore-nanopore interface resulting in large concentration gradients and clustering of ions as shown in Fig. 4(d). The interaction of electric field with the high concentration gradients disrupts the ion flow inside the nanopore resulting in dynamical changes in the ion concentration inside the pore as shown in Fig. 4(d). Furthermore, we observe spatially inhomogeneous distribution of sodium ions near the micropore-nanopore interface [see inset of Fig. 4(d)]. Figure 4(e) shows the sodium ion concentration distribution

for a low bias voltage of 5 V and for $R = 4$. In this scenario, we observe 43 times enrichment of ionic concentration near the drain-nanopore interface compared to the bulk reservoir. Also, the enrichment of ions is 1.4 times higher than $R = 20$. This suggests that concentration distribution inside the nanopore varies nonmonotonically with R resulting in nonmonotonic current dependence with R as discussed before. Further, the depletion of ions for $R = 20$ is relatively weaker than for $R = 4$ for the same applied voltage. The degree of oscillation of ions near the enriched interface is weaker for $R = 4$ [see inset of Fig. 4(e)] compared to the $R = 20$ case, resulting in higher current oscillations in the latter. Furthermore, our simulations reveal that the oscillations in the enriched zone becomes stronger on the application of high bias voltage of 100 V for $R = 4$ [see inset of Fig. 4(f)]. This is because the high electric field strongly interacts with the enriched concentration gradients disrupting the ion dynamics near the interface. We observe 80-fold enrichment of ions near the drain-nanopore interface for an applied voltage of 100 V.

Current oscillations in nanoporous membranes have been observed before by other researchers [21–26]. In many of these works, the chaotic current oscillations have been attributed to convective instability, which arises due to the irregular

movement of ionic charges and hydrodynamic flow [21,22]. Depletion of ions near one of the interfaces of an ion selective membrane with symmetric reservoirs results in a finite net space charge density and nonuniform electric field near the interface. The strong electric field combined with the net space charge density results in a nonequilibrium electroosmotic flow. Under the action of a large applied bias, the electroosmotic flow becomes unstable resulting in chaotic flow dynamics [21,22]. In our work we do not include the hydrodynamic term as we had identified from our earlier work that the contribution of electroosmotic flow is small in the calculation of the total electric current in micropore-nanopore integrated systems [29,36]. Hence, convective instability due to hydrodynamic flow is absent in our model and is not the reason for chaotic current oscillations.

Another kind of convective instability that has been shown in ion-selective systems is electro-convective instability [23–26]. This instability also occurs due to the depletion of ions developed at one of the interfaces of an ion-selective membrane. The depletion region results in high concentration gradients. Under a large bias, the electro-neutrality in the depletion region breaks resulting in a net space charge density region. On further increase in the applied voltage, the space
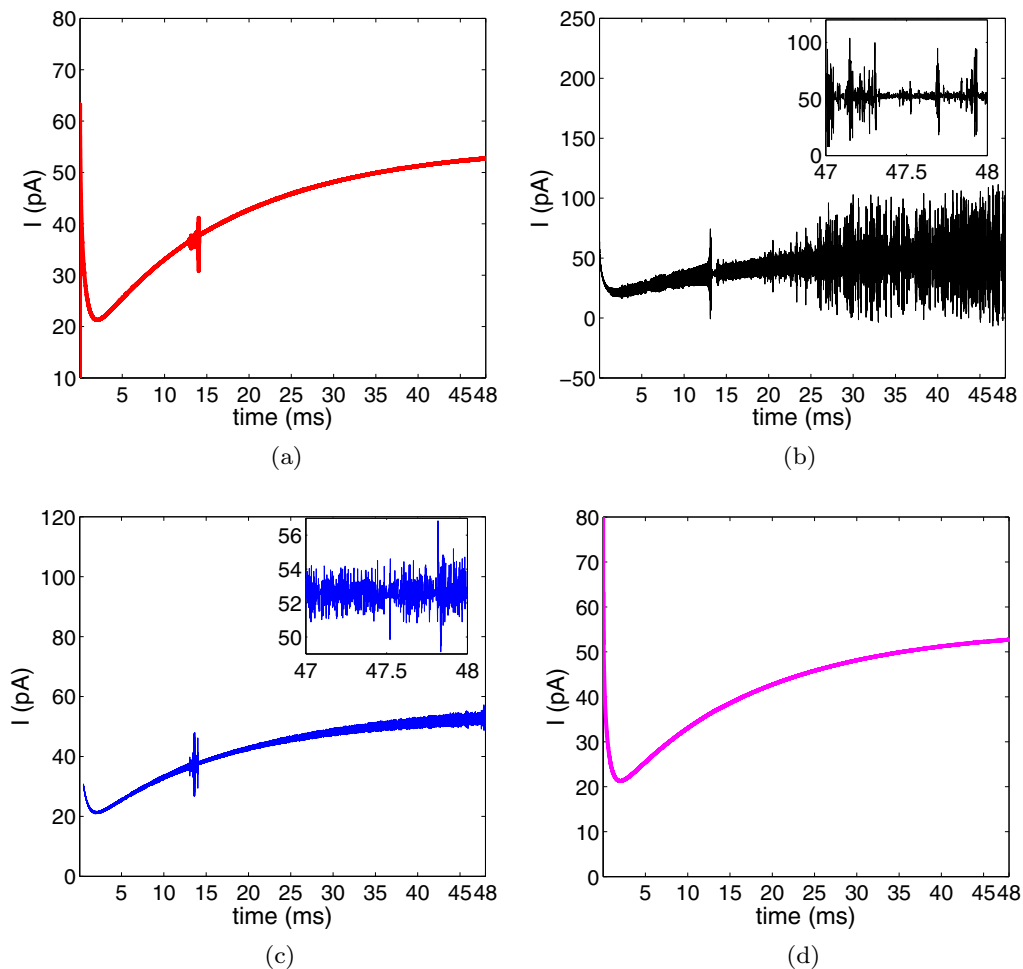

FIG. 5. Current-time dynamics at (a) bulk micropore ($x = 1\,\mu$m), (b) nanojunction ($x = 6.5\,\mu$m) (c) center of nanopore ($x = 9\,\mu$m), (d) bulk macropore ($x = 13.5\,\mu$m). The macropore reservoir diameter is 0.2 μm, micropore reservoir diameter is 0.05 μm. Ratio of macropore to micropore reservoir is 4. The applied voltage is 100 V.
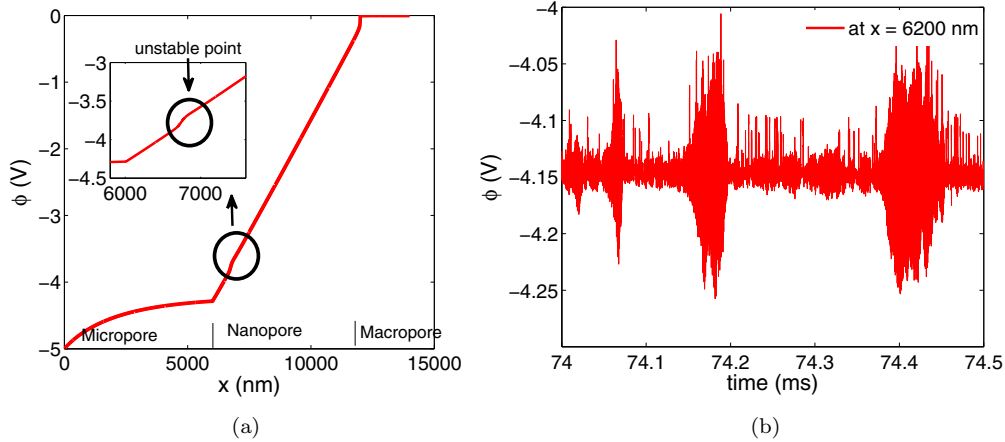
FIG. 6. Variation of potential (a) along the micro-nano-macropore system. The inset reveals the unstable potential distribution near the enriched micropore-nanopore interface (b) with time near the enriched micropore-nanopore interface. The macropore reservoir diameter is $1\,\mu$m, micropore reservoir diameter is $0.05\,\mu$m. Ratio of macropore to micropore reservoir is 20. The applied voltage is 5 V.

charge density in the depletion region becomes unstable, resulting in chaotic oscillations of electric current [23–26]. In our work the depletion region is very weak as it occurs at the nanopore-macropore reservoir, and the macropore reservoir diameter is large. We observe a very small net space charge density, with no instability, at the nanopore-macropore interface even under the action of a large applied bias. Thus, our results indicate that electro-convective instability due to depletion of ions is not the origin of chaotic current oscillation in asymmetric micro-nano-macropore systems.

In asymmetric micro-nano-macropore systems, we observe an instability of charges near the drain micro-nanojunction where the ions are enriched. This charge instability owing to the clustering of ions propagates into the nanopore and disrupts the charge distribution inside the nanopore. This observation is significant in the field of ion-selective membranes, as oftentimes the enriched region is considered inconsequential in predicting the dynamics of ionic current. Wang *et al.* [11] experimentally observed current oscillations in nanoporous membranes integrated to asymmetric fluidic reservoirs. The origin of the current oscillations was postulated to be electro-convective instability in the depleted macropore. However, concrete evidence of this mechanism was not postulated due to the lack of experimental data. We believe the present article reveals the actual mechanism of current oscillations in such asymmetric reservoir systems. We also note that the instabilities in current are local in nature; i.e., the oscillations are strong in the vicinity of the enriched micropore-nanopore interface [see Fig. 5(b)] and to an extent inside the nanopore [see Fig. 5(c)]. Away from the micropore-nanopore interface, near the bulk micropore region, the oscillations die out [see Fig. 5(a)]. Also, in the bulk macropore region, the current has steady-state characteristics [see Fig. 5(d)], owing to the absence of clustering of ions at these regions. The electric potential at each time instant can be related to the concentration by Eq. (8). We observe an unstable point in the electric potential distribution near the drain micropore-nanopore interface as shown in Fig. 6(a). Figure 6(b) shows the oscillating behavior of the unstable potential near the drain micropore-nanopore interface (at $x = 6200$ nm). A combination of dynamic clus-

tering of ions near the drain micropore-nanopore interface and the presence of unstable potential regions at this interface results in unstable current oscillations.

C. Power spectral density (PSD)

The current oscillations are examined by computing the power spectral density (S_I) in the frequency range between 0 and 50 MHz. The power spectral density is computed using the Welch method [39]. We considered a 6 ms current trace (ensuring that the current oscillates about a steady mean) to calculate the spectra. The current signal is divided into the longest possible sections to obtain close to but not exceeding eight segments, with 50% overlap. Each section is windowed with a Hamming window. The signal is sampled with a sampling frequency (f_s) of 100 MHz. The modified periodograms are averaged to obtain the spectral estimate for a frequency range $[0 - f_s/2]$. Figure 7(a) shows power spectra of a chaotic current trace for 100 V and for $R = 4$. The power spectra reveal a power-law dependence, $1/f^\alpha$ scaling in the low-frequency range between 100 kHz and 10 MHz. The exponent α is found to be close to 1 for the 100 V current signal. The inset of the figure reveals S_I for a lower voltage of 70 V and for $R = 4$. The power spectra are similar to the 100 V results and the spectra scale close to $1/f$ in the same frequency range. Figure 7(b) shows the power spectra of the simulated current-time signal for a macropore diameter of $1\,\mu$m ($R = 20$). The power spectra for this chaotic current signal scale as $1/f^\alpha$ with α close to 2, in the low-frequency range between 10 kHz and 1 MHz. The inset of the figure reveals the spectral estimate for a macropore diameter of $0.5\,\mu$m ($R = 10$). The power spectra are similar to the $1\,\mu$m case. A low bias voltage of $\phi_{DC} = 5$ V is applied in these simulations. These results indicate that power spectral density analysis can help identify voltage dominant chaos or reservoir asymmetry dominant chaos.

V. CONCLUSIONS

In this work we performed a detailed numerical study of a nanopore connected to fluidic reservoirs of asymmetric
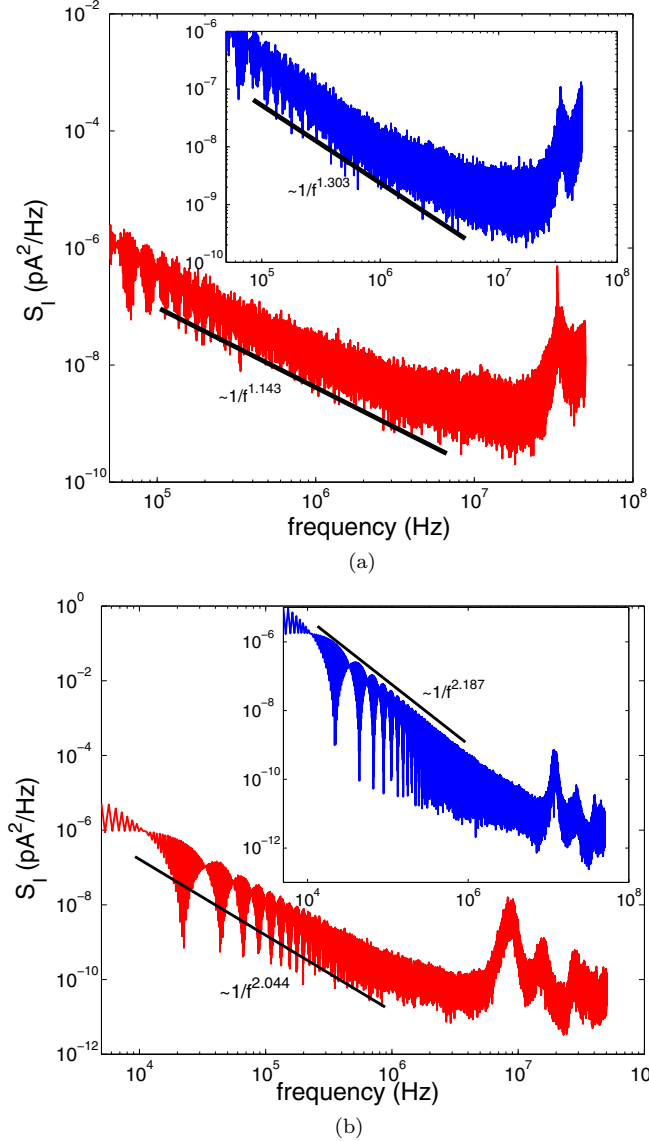
FIG. 7. Power spectral density (PSD) analysis for (a) an applied voltage of 100 V, inset shows PSD for 70 V, $R = 4$ is used for both the applied voltages; (b) a macropore diameter of 1 μm, inset shows PSD for a macropore diameter of 0.5 μm. The applied voltage is 5 V.

geometries. The micro-nano-macropore system exhibits local nonequilibrium chaotic motion of ions under the action of an applied electric field. Chaotic currents arise due to the dynamic clustering of ions, resulting in the creation of an avalanche zone, near the drain micropore-nanopore interface. Power spectral density analysis of current oscillations indicate $1/f$-type dynamics for the voltage dominant chaos and $1/f^2$-type dynamics for the reservoir asymmetry dominated chaos. The current chaos is also quantified by calculating the Lyapunov exponent of the growth rate of current dynamics. Our results indicate that reservoir asymmetry plays a pivotal role, compared to the magnitude of the applied voltage, in determining current oscillations and chaos in nanoporous systems. The results presented here can help improve the design of ionic diodes and electroosmotic pumps using asymmetric reservoir-nanopore systems.

APPENDIX: ALGORITHM TO DETERMINE THE MAXIMUM LYAPUNOV EXPONENT

The maximum Lyapunov exponent is used to determine the stability and growth of the current signal. The maximum Lyapunov exponent is calculated using four steps, outlined below.

Step 1: Construction of $\vec{I}_n$

Given n scalar time series data of the current, I_n, we convert the scalar data into state vectors by the method of delays. $\vec{I}_n$ is given by

$$\vec{I}_n = (I_0, I_1, I_2, \ldots, I_{n-(m-1)\tau}, \ldots, I_n), \qquad (A1)$$

where the dimension m and time delay τ are unknowns. It needs to be ensured that the current time signal I_n, has n time signal steps with $n > (m-1)\tau$ and $m \neq 0, 1$. Taken's embedding theorem [37] states that an optimal choice of m and τ would ensure that the geometrical object formed by the vector $\vec{I}_n$ is equivalent to the original current time signal, I_n. The above argument is guaranteed if m is larger than twice the correlation dimension, D [40], the number of active degrees of freedom. However, when we start to analyze the current time signal data, we do not know D, m, or τ. We calculate all the three variables in the next steps.

Step 2: Mutual information analysis to determine time delay, τ

To determine the optimal time delay τ, we employ the time delayed mutual information analysis developed by Fraser and Swinney [41]. To this end, we construct a 2D array $H[i][j]$, where $h1[i]$ refers to the current time data in the ith interval, and $h2[j]$ refers to the current time data in the jth interval, with $i = 1, 2, 3, \ldots, n$ and $j = i - \tau$. $H[i][j]$ refers to the current time data at the (i, j)-th interval. The mutual information S is given by

$$S(\tau) = -\sum_{ij} p_{ij}(\tau) \ln \frac{p_{ij}(\tau)}{p_i p_j}, \qquad (A2)$$

where p_i is the probability to find $h1[i]$ data signal in the ith interval, p_j is the probability to find $h2[j]$ data signal in the jth interval, and p_{ij} is the joint probability that the $H[i][j]$ data signal falls into the $(i, j) - $ th interval. The mutual information S is calculated for different choices of τ. The first minima of the mutual information, $S(\tau)$, results in the value of τ. However, when there is no minima in the mutual information, τ is taken to be 1. There is no mathematical proof associated with this statement. The mutual information, S, and time delay, τ, are obtained using the TISEAN software package [37].

Step 3: Embedding dimension, m

The embedding dimension, m, is determined in terms of the correlation dimension, D [42]. To calculate the correlation

dimension, we compute the correlation sum,

$$C(\epsilon) = \frac{1}{N_{\text{pairs}}} \sum_{j=m}^{n} \sum_{k<j-w} \Theta\big(\epsilon - |I_j - I_k|\big), \quad (A3)$$

where $N_{\text{pairs}} = (n - m + 1)(n - m - w + 1)/2$ is the number of pairs of points covered by the sum, Θ is the Heaviside step function, and ϵ is the smallest distance between two current time data points and we choose different values of ϵ. In the limit of an infinite amount of data ($n \to \infty$), and for small ϵ, we can expect C to scale like a power law, $C(\epsilon) \propto \epsilon^D$, and we can define the correlation dimension D by

$$d(n,\epsilon) = \frac{\partial \ln[C(\epsilon,n)]}{\partial \ln \epsilon}, \quad (A4)$$

$$D(\epsilon,m) = \lim_{\epsilon \to 0} \lim_{n \to \infty} d(n,\epsilon). \quad (A5)$$

To determine D, we check for the convergence of D for different values of m. w is typically chosen to be $w \ll n$. To provide some insight into typical values of D, the correlation dimension is determined to be $D = 2.96 \pm 0.05$ for an applied voltage of 100 V and an asymmetric reservoir ratio of $R = 4$. In determining D, ϵ was chosen to be between $3.17e - 14$ and $5.17e - 13$. The convergence of the correlation dimension was ensured for different values of m ($m = 20-40$). The embedding dimension m is typically greater than twice the correlation dimension, $m = 2D + 1$. Hence, the embedding dimension, m, for the current time series data is greater than 7. The optimal values of τ and m are used to construct $\vec{I}_n$. Once $\vec{I}_n$ is known the maximum Lyapunov exponent is determined, which is discussed next.

Step 4: Maximum Lyapunov exponent, λ^*

The notion of determining the Lyapunov exponents depends upon the dimensionality of the system. In this study, we focus only on determining the maximum Lyapunov exponent, λ^*, from the current time series data. Let $\vec{I}_{n_1}$ and $\vec{I}_{n_2}$ be two current measurements at simulation time t_0 with distance $||\vec{I}_{n_1} - \vec{I}_{n_2}|| = \delta_0 \ll 1$. Let $\delta_{\Delta t}$ be the distance some time Δt ahead between the two trajectories which are emerging from these points:

$$\delta_{\Delta t} = ||\vec{I}_{n_1+\Delta t} - \vec{I}_{n_2+\Delta t}||. \quad (A6)$$

Then λ^* is given by $\delta_{\Delta t} \approx \delta_0 e^{\lambda^* \Delta t}$; $\delta_{\Delta t} \ll 1$ and $\Delta t \gg 1$. When λ^* is positive, we observe an exponential divergence of current time series data, resulting in dynamic instability or chaos. To calculate the maximum Lyapunov exponent, λ^*, we choose a point in the vector, $\vec{I}_{n_0}$, of the time series data and select all neighbors in the vector, $\vec{I}_{n_0}$, within a distance of ϵ pertaining to the data sampling time. We compute the average over the distance of all neighbors to the reference point in the vector, $\vec{I}_{n_0}$, as a function of relative time. Let the average distance, $U(\vec{I}_{n_0}) = ||I_{n_0} - \vec{I}_{n_1}||$, be considered at time t_0 and the average distance $U(\vec{I}_{n_0+\Delta t}) = ||I_{n_0+\Delta t} - \vec{I}_{n_1+\Delta t}||$ be considered at time Δt. Now the maximum Lyapunov exponent, λ^*, over the time span Δt is computed;

$$\lambda^* = \frac{1}{\Delta t} \sum_{n_0=1}^{n} \ln\left[\frac{1}{|U(\vec{I}_{n_0})|}|U(\vec{I}_{n_0+\Delta t})|\right]. \quad (A7)$$

A positive λ^* indicates an exponential divergence of the current signal, resulting in a dynamic instability and chaos. λ^* is normalized as we consider the time scale in the units of time index of measurements and not the real time units.

[1] R. B. Schoch, J. Han, and P. Renaud, Transport phenomena in nanofluidics, Rev. Mod. Phys. **80**, 839 (2008).

[2] C. Dekker, Solid-state nanopores, Nat. Nanotechnol. **2**, 209 (2007).

[3] S. Howorka and Z. Siwy, Nanopore analytics: sensing of single molecules, Chem. Soc. Rev. **38**, 2360 (2009).

[4] O. A. Saleh and L. L. Sohn, An artificial nanopore for molecular sensing, Nano Lett. **3**, 37 (2003).

[5] Z. Chen, Y. Jiang, D. R. Dunphy, D. P. Adams, C. H. N. Liu, N. Zhang, G. Xomeritakis, X. Jin, N. R. Aluru, S. J. Gaik, H. W. Hillhouse, and C. J. Brinker, DNA translocation through an array of kinked nanopores, Nat. Mater. **9**, 667 (2010).

[6] J. J. Kasianowicz, E. Brandin, D. Branton, and D. W. Deamer, Characterization of individual polynucleotide molecules using a membrane channel, Proc. Natl. Acad. Sci. USA **93**, 13770 (1996).

[7] H. Chang, F. Kosari, G. Andreadakis, M. A. Alam, G. Vasmatzis, and R. Bashir, DNA-mediated fluctuations in ionic current through silicon oxide nanopore channels, Nano Lett. **4**, 1551 (2004).

[8] J. B. Heng, C. Ho, T. Kim, R. Timp, A. Aksimentiev, Y. V. Grinkova, S. Sligar, K. Schulten, and G. Timp, Sizing DNA using a nanometer-diameter pore, Biophys. J. **87**, 2905 (2004).

[9] S. J. Kim, S. H. Ko, K. H. Kang, and J. Han, Direct seawater desalination by ion concentration polarization, Nat. Nanotechnol. **5**, 297 (2010).

[10] S. A. Miller, K. Kelly, and A. T. Timperman, Ionic current rectification at a nanofluidic/microfluidic interface with an asymmetric microfluidic system, Lab Chip **8**, 1729 (2008).

[11] H. Wang, V. Nandigana, K. D. Jo, N. R. Aluru, and A. T. Timperman, Controlling the ionic current rectification factor of a nanofluidic/microfluidic interface with symmetric nanocapillary interconnects, Anal. Chem. **87**, 3598 (2015).

[12] Y. Kim, M. Cha, Y. Choi, H. Joo, and J. Lee, Electrokinetic separation of biomolecules through multiple nanopores on membrane, Chem. Phys. Lett. **561–562**, 63 (2013).

[13] S.-W. Nam, M. J. Rooks, K.-B. Kim, and S. M. Rossnage, Ionic field effect transistors with sub 10 nm multiple nanopores, Nano Lett. **9**, 2044 (2009).

[14] Z. Siwy and A. Fuliński, Fabrication of a Synthetic Nanopore Ion Pump, Phys. Rev. Lett. **89**, 198103 (2002).

[15] R. Karnik, C. Duan, K. Castelino, H. Daiguji, and A. Majumdar, Rectification of ionic current in a nanofluidic diode, Nano Lett. **7**, 547 (2007).

[16] M. R. Powell, I. Vlassiouk, C. Martens, and Z. S. Siwy, Nonequilibrium $1/f$ Noise in Rectifying Nanopores, Phys. Rev. Lett. **103**, 248104 (2009).

[17] R. M. M. Smeets, N. H. Dekker, and C. Dekker, Low-frequency noise in solid-state nanopores, Nanotechnology **20**, 095501 (2009).

[18] Z. Siwy and A. Fuliński, Origin of $1/f^{\alpha}$ Noise in Membrane Channel Currents, Phys. Rev. Lett. **89**, 158101 (2002).

[19] R. M. M. Smeets, U. F. Keyser, M. Y. Wu, N. H. Dekker, and C. Dekker, Nanobubbles in Solid-State Nanopores, Phys. Rev. Lett. **97**, 088101 (2006).

[20] M. R. Powell, N. Sa, M. Davenport, K. Healy, I. Vlassiouk, S. E. Létant, L. A. Baker, and Z. S. Siwy, Noise properties of rectifying nanopores, J. Phys. Chem. C **115**, 8775 (2011).

[21] C. L. Druzgalski, M. B. Andersen, and A. Mani, Direct numerical simulation of electroconvective instability and hydrodynamic chaos near an ion-selective surface, Phys. Fluids **25**, 110804 (2013).

[22] S. J. Kim, Y.-C. Wang, J. H. Lee, H. Jang, and J. Han, Concentration Polarization and Nonlinear Electrokinetic Flow Near a Nanofluidic Channel, Phys. Rev. Lett. **99**, 044501 (2007).

[23] G. Yossifon and H.-C. Chang, Selection of Non-Equilibrium Over-Limiting Currents: Universal Depletion Layer Formation Dynamics and Vortex Instability, Phys. Rev. Lett. **101**, 254501 (2008).

[24] G. Yossifon, P. Mushenheim, Y. C. Chang, and H.-C. Chang, Nonlinear current-voltage characteristics of nano-channels, Phys. Rev. E **79**, 046305 (2009).

[25] I. Rubinstein, B. Zaltzman, and I. Lerman, Electroconvective instability in concentration polarization and nonequilibrium electro-osmotic slip, Phys. Rev. E **72**, 011505 (2005).

[26] B. Zaltzman and I. Rubinstein, Electro-osmotic slip and electroconvective instability, J. Fluid Mech. **579**, 173 (2007).

[27] D. R. Parisi, D. Sornette, and D. Helbing, Financial price dynamics and pedestrian counterflows: A comparison of statistical stylized facts, Phys. Rev. E **87**, 012804 (2013).

[28] C. Saloma, G. J. Perez, G. Tapang, M. Lim, and C. P. Saloma, Self-organized queuing and scale-free behavior in real escape panic, Proc. Natl. Acad. Sci. USA **100**, 11947 (2003).

[29] V. V. R. Nandigana and N. R. Aluru, Characterization of electrochemical properties of a micro-nanochannel integrated system using computational impedance spectroscopy (CIS), Electrochim. Acta **105**, 514 (2013).

[30] H. Daiguji, P. Yang, and A. Majumdar, Ion transport in nanofluidic channels, Nano Lett. **4**, 137 (2004).

[31] R. F. Probstein, *Physiochemical Hydrodynamics: An Introduction* (John Wiley and Sons, New York, 1994).

[32] http://www.openfoam.com/, 2011.

[33] E. F. Toro, *Riemann Solvers and Numerical Methods for Fluid Dynamics* (Springer-Verlag, New York, 1999).

[34] B. Hille, *Ion Channels of Excitable Membranes*, 3rd ed. (Sinauer Associates, Sunderland, MA, 2001).

[35] W. H. Keesom, R. Zelenka, and C. Radke, A zeta-potential model for ionic surfactant adsorption on an ionogenic hydrophobic surface, J. Colloid Interface Sci. **125**, 575 (1988).

[36] V. V. R. Nandigana and N. R. Aluru, Understanding anomalous current-voltage characteristics in microchannel-nanochannel interconnect devices, J. Colloid Interface Sci. **384**, 162 (2012).

[37] H. Kantz and T. Schreiber, *Nonlinear Time Series Analysis*, 2nd ed. (Cambridge University Press, Cambridge, 2004).

[38] D. P. Hoogerheide, S. Garaj, and J. A. Golovchenko, Probing Surface Charge Fluctuations with Solid-State Nanopores, Phys. Rev. Lett. **102**, 256804 (2009).

[39] P. D. Welch, The use of fast fourier transform for the estimation of power spectra: A method based on time-averaging over short, modified periodograms, IEEE Trans. Audio Electroacoustics **AU-15**, 70 (1967).

[40] M. Ding, C. Grebogi, E. Ott, T. Sauer, and J. A. Yorke, Plateau Onset for Correlation Dimension: When Does it Occur? Phys. Rev. Lett. **70**, 3872 (1993).

[41] A. M. Fraser and H. L. Swinney, Independent coordinates for strange attractors from mutual information, Phys. Rev. A **33**, 1134 (1986).

[42] P. Grassberger and I. Procaccia, Measuring the strageness of strange attractors, Physica D **9**, 189 (1983).